The Astrophysical Journal, 977:256 (16pp), 2024 December 20 https://doi.org/10.3847/1538-4357/ad8dd8

The Redshift of GRB 190829A/SN 2019oyw: A Case Study of GRB-SN Evolution

Kornpob Bhirombhakdi[1], Andrew S. Fruchter[1], Andrew J. Levan[2,3], Elena Pian[4], Paolo Mazzali[5,6], Luca Izzo[7,8], Tuomas Kangas[9,10], Stefano Benetti[11], Kyle Medler[5], and Nial Tanvir[12]
[1] Space Telescope Science Institute, 3700 San Martin Drive, Baltimore, MD 21218, USA; bkornpob@gmail.com
[2] Department of Astrophysics/IMAPP, Radboud University Nijmegen, P.O. Box 9010, 6500 GL Nijmegen, The Netherlands
[3] Department of Physics, University of Warwick, Coventry, CV4 7AL, UK
[4] INAF, Astrophysics and Space Science Observatory, Via P. Gobetti 101, 40129 Bologna, Italy
[5] Astrophysics Research Institute, Liverpool John Moores University, 146 Brownlow Hill, Liverpool L3 5RF, UK
[6] Max-Planck Institut für Astrophysik, Karl-Schwarzschild-Straße 1, D-85748 Garching, Germany
[7] DARK, Niels Bohr Institute, University of Copenhagen, Copenhagen N, Denmark
[8] INAF—Osservatorio Astronomico di Capodimonte, Naples, Italy
[9] Finnish Centre for Astronomy with ESO (FINCA), University of Turku, FI-20014, Finland
[10] Department of Physics and Astronomy, University of Turku, Vesilinnantie 5, FI-20500, Finland
[11] INAF—Osservatorio Astronomico di Padova, vicolo dell'Osservatorio 5, Padova I-35122, Italy
[12] School of Physics and Astronomy, University of Leicester, University Road, Leicester LE1 7RJ, UK
Received 2024 March 26; revised 2024 October 12; accepted 2024 October 15; published 2024 December 18

Abstract

The nearby long gamma-ray burst (GRB) 190829A was observed using the Hubble Space Telescope/Wide Field Camera 3/infrared grisms about four weeks to 500 days after the burst. We find the spectral features of its associated supernova, SN 2019oyw, are redshifted by several thousand km s^{-1} compared to the redshift of the large spiral galaxy on which it is superposed. This velocity offset is seen in several features but most clearly in Ca II near-infrared triplet $\lambda\lambda$8498, 8542, 8662 (CaIR3). We also analyze Very Large Telescope/FOcal Reducer and low dispersion Spectrograph and X-shooter spectra of the supernova (SN) and find strong evolution with time of its P-Cygni features of CaIR3 from the blue to the red. However, comparison with a large sample of Type Ic-BL and Ic SNe shows no other object with the CaIR3 line as red as that of SN 2019oyw were it at the $z = 0.0785$ redshift of the disk galaxy. This implies that SN 2019oyw is either a highly unusual SN or is moving rapidly with respect to its apparent host. Indeed, using CaIR3 we find the redshift of SN 2019oyw is $0.0944 \leqslant z \leqslant 0.1156$. The GRB-SN is superposed on a particularly dusty region of the massive spiral galaxy; therefore, while we see no sign of a small host galaxy behind the spiral, it could be obscured. Our work provides a surprising result on the origins of GRB 190829A, as well as insights into the time evolution of GRB-SNe spectra and a method for directly determining the redshift of a GRB-SN using the evolution of strong spectral features such as CaIR3.

Unified Astronomy Thesaurus concepts: Core-collapse supernovae (304); Gamma-ray bursts (629); Spectroscopy (1558)

1. Introduction

The long-duration gamma-ray burst (GRB) 190829A (A. de Ugarte Postigo et al. 2019; V. Lipunov et al. 2019; A. Volnova et al. 2019) was detected by the Fermi Gamma-ray Burst Monitor (GBM) on 2019 August 29, 19:55:53.13 UTC (henceforth, we adopted this as T_0 for the event; Fermi GBM Team 2019), and shortly after by the Swift Burst Alert Telescope (S. Dichiara et al. 2019). Its afterglow was detected in multiple wavelengths from X-ray to radio (V. Chand et al. 2020; N. Fraija et al. 2021; Y. D. Hu et al. 2021; S. Dichiara et al. 2022; O. S. Salafia et al. 2022), and revealed its location to be superposed on the galaxy SDSS J025810.28–085719.2 (henceforth, we refer to this galaxy in short as the "SDSS galaxy"; for further information see skyserver.sdss.org; Abdurro'uf et al. 2022; also Figure 1).[13] Very high energy (VHE) photons in the tera-electronvolt range were detected from the event (M. de Naurois 2019; H.E.S.S. Collaboration et al. 2021), while the search for associated neutrinos yielded only an upper limit (ANTARES Collaboration et al. 2021). The detection of Ca II H/K $\lambda\lambda$3934, 3969 absorption in the afterglow (A. F. Valeev et al. 2019; Y. D. Hu et al. 2021) gave the redshift estimate $z = 0.0785$, which is consistent with the observed redshift of that galaxy. This bright spiral has a stellar mass of order of $10^{12}\,M_{\odot}$ (R. Gupta et al. 2022), the largest stellar mass of any proposed GRB host. The galaxy also exhibits characteristics of an active galactic nucleus (AGN; Izzo et al. 2024, in preparation; Patricia Schady via personal communication), which would be the first for a long GRB host. Moreover, the sight-line to the GRB was estimated to have $A_V = 2.33$ mag (L.-L. Zhang et al. 2021), making it unusually dusty for a long GRB environment at a redshift $z < 1$. Despite being atypical for a long GRB host (A. S. Fruchter et al. 2006; P. L. Kelly et al. 2014; D. A. Perley et al. 2016; J. Japelj et al. 2018; M. Modjaz et al. 2020), the SDSS galaxy seems to be the obvious choice considering the location of the burst and the fact that all observed absorption features in the GRB spectrum appear to come from this galaxy.

Perhaps in part because it was so nearby, GRB 190829A itself was found to have a number of somewhat unusual properties. For example, the Amati correlation, which typically characterizes long GRBs (L. Amati 2006), was violated by one but not another of two main emission events from this burst

[13] This SDSS galaxy is also known as 2MASX J02581029–0857189 (M. F. Skrutskie et al. 2006).

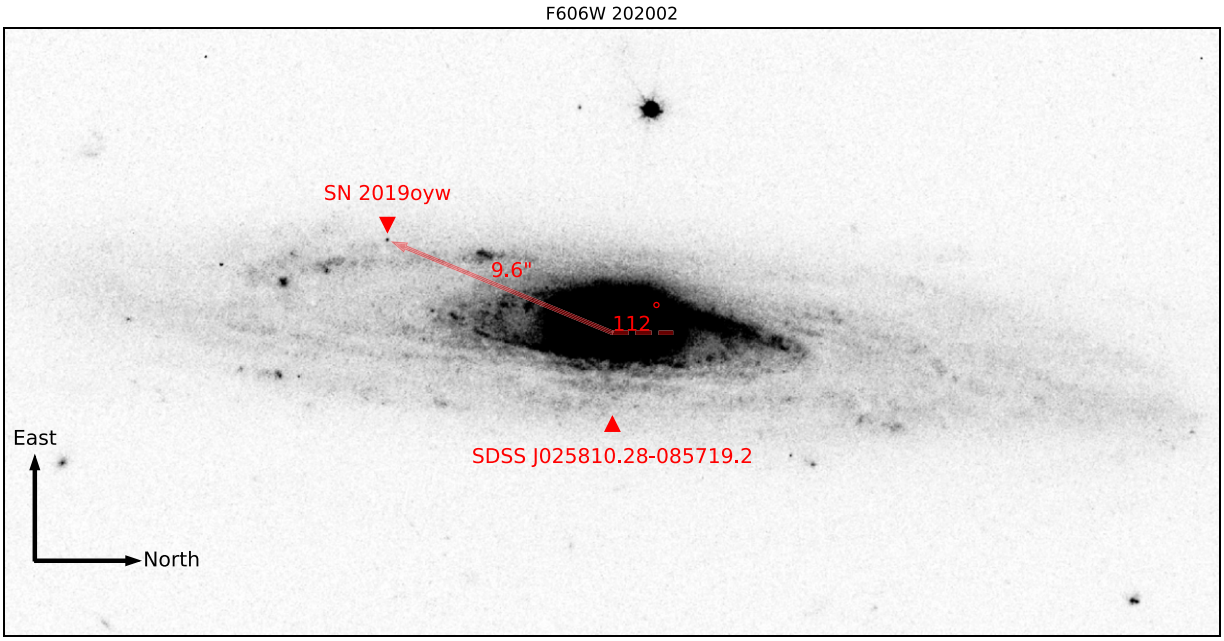

Figure 1. Image of SN 2019oyw superposing on the outer disk of SDSS J025810.28–085719.2. This image was taken with HST/WFC3/UVIS/F606W on 2020 February 16. SN 2019oyw was $\sim 10''$ from the brightest pixel at the galactic center in the direction $\sim 112°$ with respect to north toward southeast.

(V. Chand et al. 2020). Although it was a VHE burst displaying photons with energy above 100 GeV, its peak photon energy was among the lowest of known VHE-GRBs (see Y. Sato et al. 2023 and references therein). It also had the smallest isotropic energy when compared to other VHE-GRBs (H. Abdalla et al. 2019; M.-Y. Duan & X.-G. Wang 2019; MAGIC Collaboration et al. 2019; M. E. Ravasio et al. 2019; O. Blanch et al. 2020).

However, it is the supernova associated with the GRB 190829A, SN 2019oyw, which most interests us in this paper. SN 2019oyw emerged a few days after the GRB trigger (A. de Ugarte Postigo et al. 2019; V. Lipunov et al. 2019; A. Volnova et al. 2019), and reached its *i*-band peak by $\sim$20 days (Y. D. Hu et al. 2021). Its early spectra showed characteristic features of a type Ic-BL (N. Fraija et al. 2021; Y. D. Hu et al. 2021), similar to other GRB-SNe (Z. Cano et al. 2014; M. Modjaz et al. 2016) and in particular the prototype GRB-SN 1998bw (F. Patat et al. 2001). Broad absorption features of Si II λ6355 and the Ca II near-infrared (NIR) triplet $\lambda\lambda$8498, 8542, 8662 (henceforth CaIR3, using the terminology of J. M. Silverman et al. 2015) were identified (Y. D. Hu et al. 2021).

In this paper (Section 2), we present late-time observations of SN 2019oyw from Wide Field Camera 3 of the Hubble Space Telescope (HST/WFC3) observed between 2019 September 28 and 2021 January 9 (i.e., 30–499 days after the trigger in the observing frame). Optical and NIR images and NIR grism data were obtained. Our analysis of these data (Section 3) shows that the spectral features associated with the supernova at late time ($\sim$50 days) are redshifted by several thousands of km s^{-1} compared to the redshift of the large spiral on which it is superposed. With additional data from the Very Large Telescope (VLT) provided by K. Medler (2023) and Izzo et al. (2024, in preparation), we analyze spectral features of the supernova together with a sample of GRB-SNe, SNe Ic-BL (without associated GRB), and SNe Ic, and show that SN 2019oyw is the only outlier (Section 4). We re-estimate the redshift that improves the feature alignment, and interpret this as surprising evidence that the supernova (SN) progenitor exploded in or near the SDSS galaxy with a great peculiar velocity, or it was hosted by another galaxy of the order 100 Mpc behind the SDSS galaxy (Section 5). However, we find no evidence of another more distant host in the spectra or images, while the nondetection still does not rule out the possibility. Finally, we summarize our results in Section 6.[14]

2. Observations

GRB 190829A/SN 2019oyw was observed at several epochs between 2019 September 28 and 2021 January 9 (i.e., 30–499 days after the trigger in the observing frame) by the HST/WFC3 (L. Dressel 2021). Both images and spectra were obtained in optical and NIR, as summarized in Table 1. In this section, we briefly describe the data and the reduction process for photometry and spectroscopy from the HST, in Sections 2.1 and 2.2, respectively. In addition to the HST data, we were provided additional data from the VLT by K. Medler (2023) and Izzo et al. (2024, in preparation). We briefly describe the VLT observations in Section 2.3.

2.1. HST/WFC3 Photometry

Images of SN 2019oyw were taken by HST/WFC3 (L. Dressel 2021) in optical (UVIS channel) and NIR (IR channel). Table 1 summarizes the data. We followed the reduction process recommended by K. C. Sahu et al. (2021). The data were preprocessed and downloaded from the Barbara A. Mikulski Archive for Space Telescopes (MAST; https://archive.stsci.edu/) in FLT/FLC format. The dithered images were combined using Drizzle (A. S. Fruchter & R. N. Hook 2002) as implemented in ASTRODRIZZLE (Gonzaga).[15] Figure 1 shows an example of the processed image from F606W on 2020 February 16. The image clearly shows SN 2019oyw

[14] We assume a ΛCDM cosmology with $H_0 = 70$ km s^{-1} Mpc^{-1}, $\Omega_m = 0.3$, $\Omega_\Lambda = 0.7$.
[15] https://www.stsci.edu/scientific-community/software/drizzlepac.html

Table 1
Summary of Datasets from HST/WFC3

Proposal ID (1)	PI (2)	Epoch (3)	Channel (4)	Filter (5)	Total Exposure (s) (6)
15089	E. Troja	2019-09-28	IR	F110W[a]	148
				F160W[a]	148
				G102	2012
				G141	2012
		2019-10-26	IR	F110W[a]	148
				F160W[a]	148
				G102	2012
				G141	2012
15510	N. Tanvir	2019-11-25	UVIS	F606W	870
				F814W	870
		2019-11-29	IR	F105W[a]	349
				F125W[a]	349
				F140W[a]	698
				G102	4095
				G141	4095
		2020-01-12	UVIS	F606W	900
				F814W	900
			IR	F105W[a]	349
				F125W[a]	349
				F140W[a]	349
				G102	4095
				G141	4095
16042	A. Levan	2020-02-11	IR	F125W[a]	698
				F140W	1198
				G102	4095
				G141	4095
		2020-02-16	UVIS	F606W	1044
		2020-06-24	UVIS	F606W	1044
			IR	F140W	1198
		2020-08-21	UVIS	F606W	1044
			IR	F140W	1198
16320	A. Levan	2021-01-09	UVIS	F606W	1044
			IR	F125W[a]	698
				F140W[a]	1746
				G102	4095
				G141	4095

Notes. All of the data presented in this table were obtained from the MAST at the Space Telescope Science Institute. The specific observations analyzed can be accessed via doi:10.17909/yz9m-xb66.
[a] Indicates that images taken with grism observations were included. See L. Dressel (2021) for details.

superposed on the outer disk of the SDSS J025810.28–085719.2 (S. Dichiara et al. 2019; S. R. Oates et al. 2019; Y. D. Hu et al. 2021).

To perform the photometric measurement, we removed the galaxy light by template subtraction for filters F606W, F125W, and F140W where we used the observations on 2021 January 9 (499 days) as templates. We show in Figure 2 an example of the original source image (left-hand panel), template image (middle panel), and the result from the subtraction (right-hand panel). The alignment was done by using nearby stars in a subset of the field-of view. The stellar alignments were accurate to the order of 0.1 pixel. We note that some complications were met when reducing some of these data. For F140W, 2020 February 11, we only combined the observations dedicated for imaging and excluded the direct images associated with G141 grism observation. This is because the direct images associated with the grism were taken using a different part of the chip and the distortion solutions are sufficiently inexact that the overall subtraction is better without these data, even though the total integration is somewhat shorter by excluding them (i.e., 1200 versus 1900 s). For F140W, 2020 June 24, there was scattered light from out of the field, causing the estimated upper limit to be brighter than it would have been in an uncontaminated part of the field.

For the other filters where we did not observe a template, we modeled the image around the source with two components: a point source as a 2D Gaussian for the transient component and the galaxy component as a smooth background modeled by a low-order polynomial. We implemented this using the ASTROPY package (Astropy Collaboration et al. 2013, 2018). Figure 3 shows an example of the described procedure. From the source image (left-hand panel), the two-component model was fitted to the data given a region centered on the transient. We used the background component (middle panel) for the subtraction (right-hand panel).

We note that in the template images (Figure 4) a clump, located slightly to the north and west of the SN, is noticeable in F125W and F140W, but is less noticeable in F606W. Our background models with low-order polynomials cannot capture the clump. However, the method was only applied to

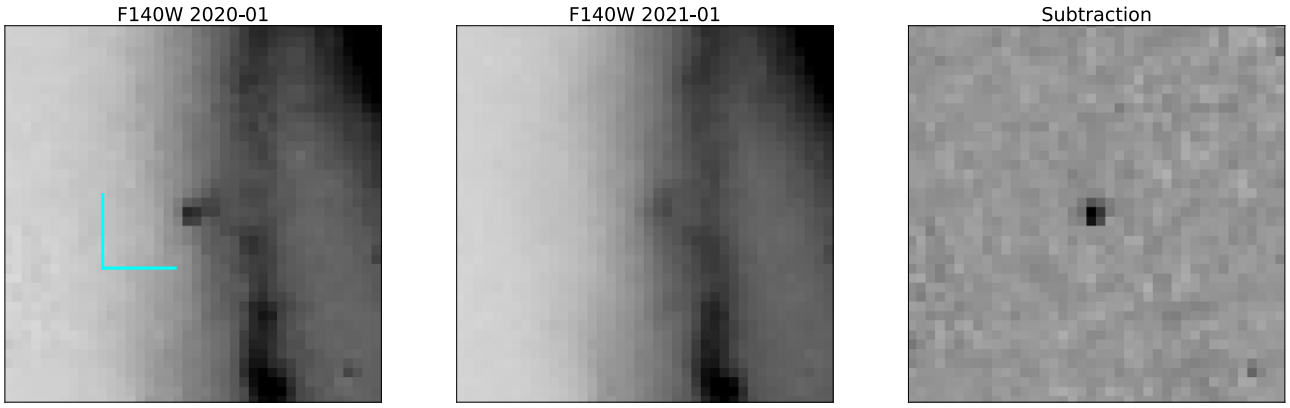

Figure 2. Images of SN 2019oyw from F140W filter. The source image taken on 2020 January 12 (left-hand panel) was subtracted by the template image taken on 2021 January 9 (middle panel), resulting in the subtracted image (right-hand panel) that clearly shows the transient. These images are shown in inversed-color (i.e., black = bright). Orientation is north-up and east-left. The cyan lines show the length scale of 1″ in each direction.

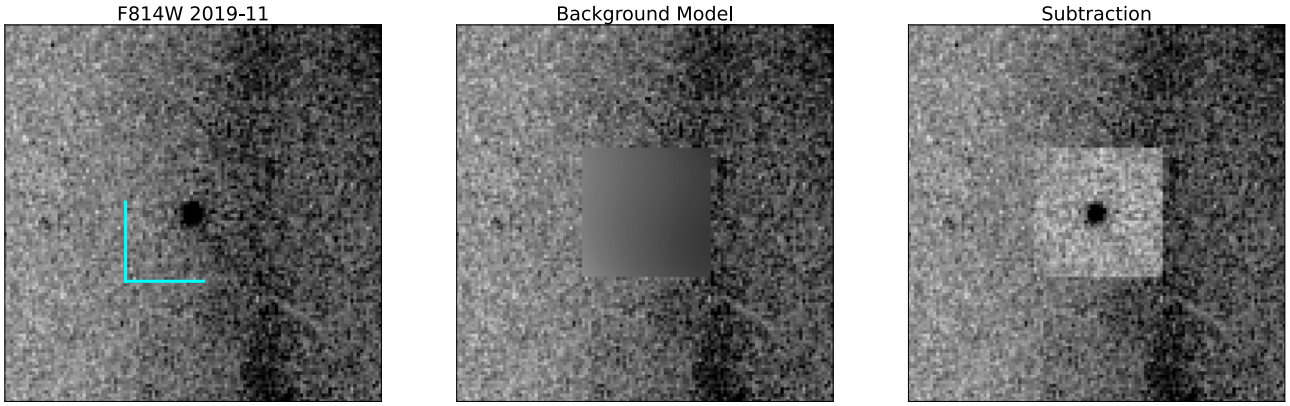

Figure 3. An image of SN 2019oyw taken by HST/WFC3/UVIS/F814W on 2019 November 25 (left-hand panel). Its background model is shown in the middle panel, resulting in the subtraction image in the right-hand panel. These images are shown in inversed-color (i.e., black = bright). Orientation is north-up and east-left. The cyan lines show the length scale of 1″ in each direction.

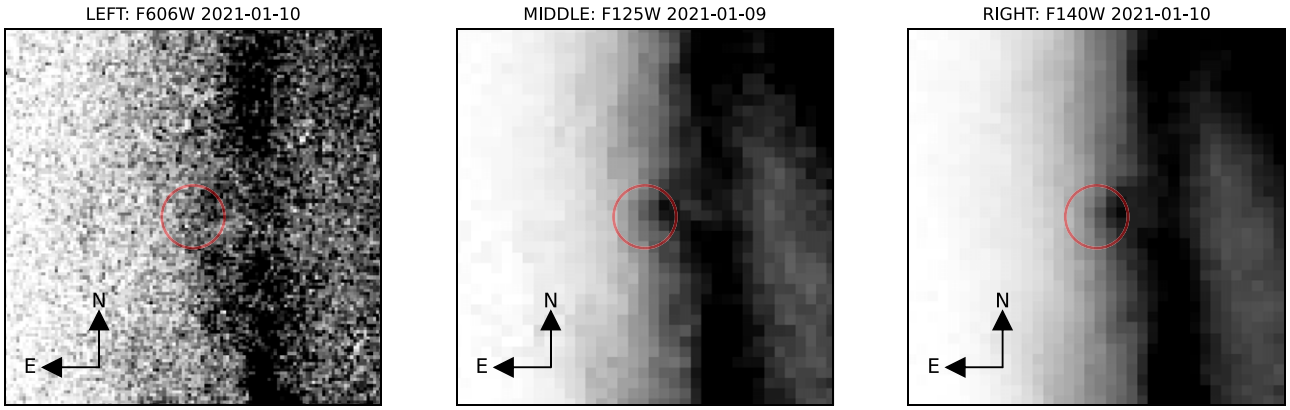

Figure 4. Environment of GRB 190829A/SN 2019oyw in F606W, F125W, and F140W. Images were taken in 2021 January, and are shown in inverse color, i.e., black = bright. The event was located at the center. Each red circular aperture is the size of 0.″39 in radius (i.e., 3 pixels in WFC3/IR and 9.75 pixels in WFC3/UVIS images). We observed a dust lane extending from north to south westwards from the aperture. We noted a bright clump (noticeable especially in F125W and F140W) associated with the dust lane on the western edge of the aperture.

observations from epochs 2019 September to 2020 January, when the transient was visibly brighter than the background. To estimate the uncertainties, in order to compare with the template subtraction method, we repeated the reduction process with images on 2020 January in F606W, F125W, and F140W by applying a background modeling method. We found that the subtracted images from the background models are consistently undersubtracted, when compared to the template subtraction. The difference of the photometric measurements between the two methods is about 6.5% (F606W), 13.4% (F125W), and 32.6% (F140W). Since the F814W and F105W images on 2020 January were processed by the background modeling method, the uncertainties of these photometric measurements should be approximately 10% (if assuming a monotonic trend of the

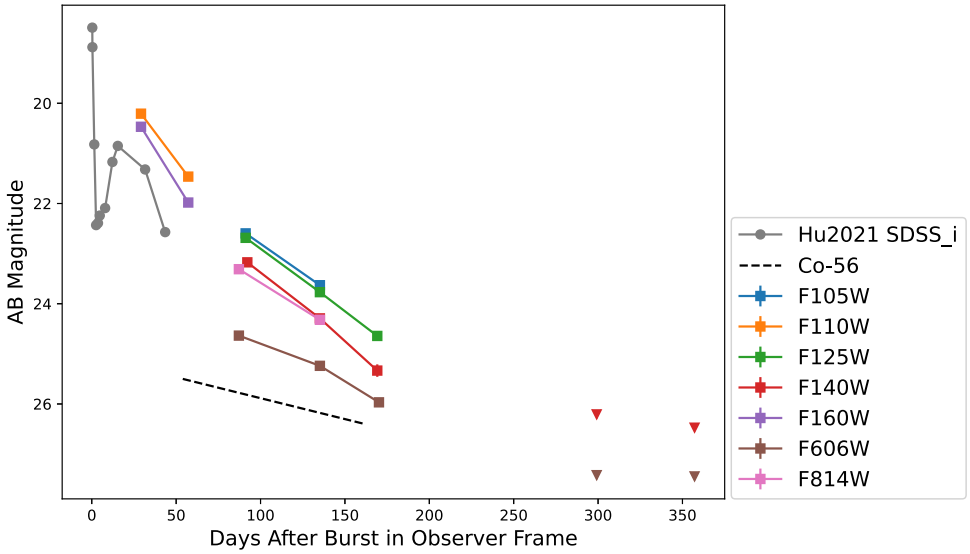

Figure 5. Light curves of SN 2019oyw. From the late-time observations, data points are squares for detections and triangles for 3σ upper limits. For comparison, the plot also shows observations presented in Y. D. Hu et al. (2021) in SDSS's *i*-filter (gray dots), and the expected light curve's slope if powered by fully trapped Co^{56} (black dashed line). These values are uncorrected for Galactic and extragalactic extinction.

Table 2
Photometry of SN 2019oyw

Filter	2019-09	2019-10	2019-11	2020-01	2020-02	2020-06	2020-08
F606W	⋯	⋯	24.64(0.03)	25.24(0.04)	25.97(0.08)	>27.42	>27.45
F814W	⋯	⋯	23.31(0.02)	24.32(0.04)	⋯	⋯	⋯
F105W	⋯	⋯	22.60(0.02)	23.63(0.04)	⋯	⋯	⋯
F110W	20.21(0.00)	21.46(0.01)	⋯	⋯	⋯	⋯	⋯
F125W	⋯	⋯	22.69(0.02)	23.77(0.05)	24.64(0.09)	⋯	⋯
F140W	⋯	⋯	23.17(0.02)	24.29(0.05)	25.33(0.12)	>26.21	>26.47
F160W	20.47(0.01)	21.98(0.03)	⋯	⋯	⋯	⋯	⋯

Note. Units are in AB-magnitude. One-sigma uncertainties are in parentheses. Upper limits are 3σ above zero. These values are uncorrected for extinction. Epochs are shortened to only YYYY-MM format for better readability. Note that for F606W, F125W, and F140W we used the epoch 2021 January as a template for host subtraction, while background models were used for the other filters (see Section 2.1). Due to the lack of templates for filters F814W, F105W, F110W, and F160W, we estimate systematic uncertainties to be about 10% on epoch 2020 January, and should be proportionately less for earlier epochs. See text.

uncertainties considering the observed wavelengths). For the 2019 October epoch of F160W, we also estimate an error of ∼10%.

Aperture photometry was performed using the PHOTUTILS package (L. Bradley et al. 2020).[16] An aperture with radius of 3 pixels was used for WFC3/IR observations (i.e., ∼0.″39), and 4 pixels for UVIS (i.e., ∼0.″16). Aperture correction (from finite to infinite aperture) was done following the tables given in L. Dressel (2021). For a nondetection, we report a 3σ upper limit (above zero) instead. Uncertainties were propagated for the template subtraction, while we assumed negligible uncertainties from the low-order polynomial background model. Table 2 summarizes the photometry in apparent AB-magnitude. Figure 5 shows the light curve.

The data shows SN 2019oyw fading continuously until the last detection on 2020 February 16 (171 days after trigger in the observer's frame). In the figure, we additionally show the early *i*-band light curve from Y. D. Hu et al. (2021) for comparison (in gray), which shows a consistent decline from the *i*-band peak. We note that the SDSS *i*-band is approximately comparable to the F814W of HST/WFC3. The decline rates from NIR bands are about 0.05 mag day^{-1} in observing frame between 2019 September (29 days) and 2019 October (57 days), which is slower than the optical decline rate implied by the *i*-band. Then, the decline rates become slower at later times in both optical and NIR. SN 2019oyw evolved as expected for a typical GRB-SN by showing the late-time decline rates being consistent with being powered by ^{56}Co with the γ-rays not fully trapped (T. Nakamura et al. 2001; S. E. Woosley & J. S. Bloom 2006).

2.2. *HST/WFC3 Spectroscopy*

The spectroscopic observations of SN 2019oyw were observed by grisms G102 (8000–11500 Å) and G141 (10750–17000 Å) with the WFC3/IR channel (L. Dressel 2021) in six epochs (see Table 1). We reduced the data using the recommended grism reduction procedure (K. C. Sahu et al. 2021) and the Python version of the HSTAXE package.[17] In

[16] https://photutils.readthedocs.io/en/stable/

[17] https://www.stsci.edu/scientific-community/software/axe

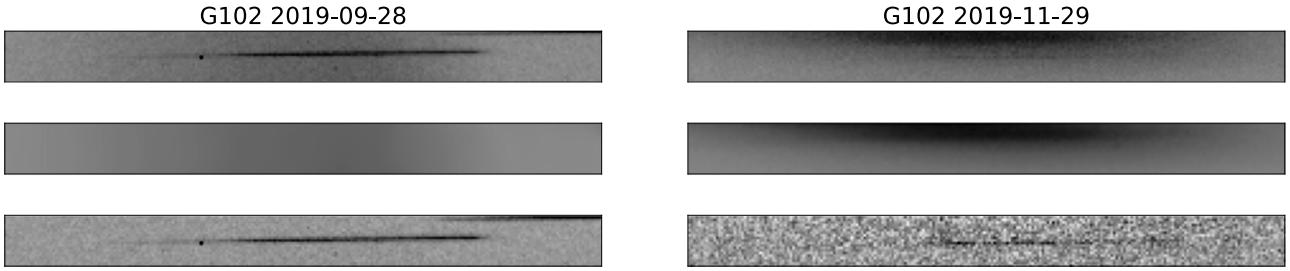

Figure 6. Grism images of SN 2019oyw and their background subtractions. Left-hand panels: G102 image on 2019 September 28 (top panel), its background model (middle panel), and subtraction image (bottom panel). Right-hand panels: G102 image on 2019 November 29 (top panel), its background template from epoch 2021 January 9, and subtraction image (bottom panel). These images are shown in inversed-color (i.e., black = bright).

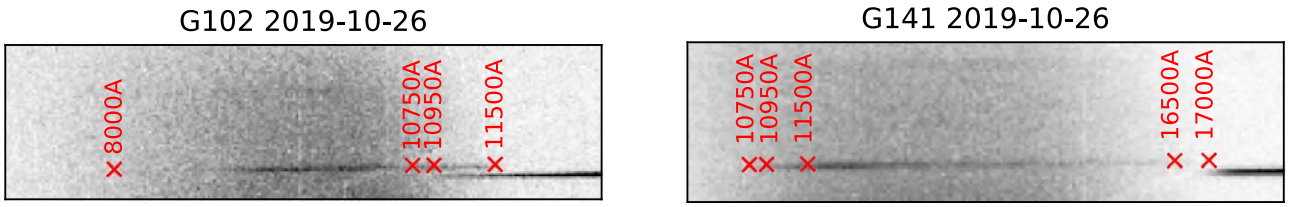

Figure 7. Grism images on 2019 October 26 epoch in G102 (left-hand panel) and G141 (right-hand panel). Red markers mark corresponding wavelengths on SN 2019oyw's traces. We note the markers 10750 and 11500 Å specifying the overlapping region between both filters. Another trace, which is visible in the bottom right-hand corner of each image, was from another nearby star. The vertical separation along *y*-axis of the traces is 4 pixels in both filters. For G102, the star's trace contaminates starting at 10950 Å. For G141, SN 2019oyw's trace is truncated at the red end due to low signal-to-noise ratio, and for this epoch we could extract meaningful information up to about 16500 Å, where the contamination is insignificant. We note also the truncation of the spectrum at the blue end on G102 due as well to low signal-to-noise ratio.

brief, the preprocessed data in FLT format can be downloaded from MAST (https://archive.stsci.edu/). With the source's location known from the associated direct images, the software can identify the source's trace and calibrate its wavelengths in the grism images. The reduction procedure continues by performing flat-field calibration, modeling and subtracting the background around the target's trace, extracting the 1D spectrum, and calibrating the fluxes. We also used the recommended axedrizzle function (M. W. Kuemmel et al. 2005) to coadd spectra from dithered observations.

The templates observed on 2021 January 9 were performed with approximately the same spacecraft orientation as the observations on 2019 November 29 and 2020 January 12 to simplify and optimize the spectral template subtraction. (We note that the source was not detected on the epoch 2020 February 6). We used DRIZZLEPAC to generate the master template by co-adding dithered images of the template and blotted the master template back to the orientation of each source image. Then, the blotted image was subtracted from the source image. The resulting image was then used in HSTAXE for the reduction of the 1D spectrum. The right-hand panels in Figure 6 show an example of this procedure: the source image (top panel), the master template (middle panel), and the resulting image from subtraction (bottom panels).

For observations on 2019 September 28 and 2019 October 26, we did not observe templates for subtraction. The light contamination, mainly contributed by the SDSS galaxy, was removed by modeling. To do this, since the developer's version of the HSTAXE (which we had access to) did not have the routine for "local background" estimation available, we instead used the package HSTGRISM (https://pypi.org/project/hstgrism/), which can perform this task in a similar fashion. The local background estimation (see also https://github.com/spacetelescope/hstaxe) specifies a mask over the target's trace. Then, given pixels above and below the trace mask at each wavelength (i.e., along *X*-axis), it performs 1D interpolation in the cross-dispersion direction (i.e., along *Y*-axis) assuming a low-order polynomial model. Then, a 2D Gaussian smoother is applied over the estimated background region to reduce the noises. Our best estimate specifies the trace mask of 7 pixels (in *Y*-axis, centered on the trace), polynomial order 2, and 3 pixels for the 2D Gaussian's sigma. The left–hand panels in Figure 6 show an example of this procedure: the source image (top panel), the background model (middle panel), and the resulting image from subtraction (bottom panel).

After the galaxy-light removal, the resulting images were used as inputs to the HSTAXE. We configured the software so that the HSTAXE performed a simple box extraction and coadded using axedrizzle. We obtained the 1D spectra with uncalibrated fluxes due to the finite aperture. To calibrate to the infinite-aperture values, we adopted the aperture correction presented in H. Kuntschner et al. (2011).

We also examined contamination from other nearby sources. There is a trace of a bright star locating near the red tails of the source's traces for both G102 and G141 on epochs 2019 September 28 and 2019 October 26. However, the contamination was insignificant. Specifically, on 2019 September 28 the stellar trace is well-separated from that of the GRB-SN (see Figure 6 left-hand panels; the star's trace is shown on the top right-hand corner of the figure). For 2019 October 26, the contamination was also not a problem as shown in Figure 7. For G102 (Figure 7, left-hand panel), the contamination starts around 10950 Å. We corrected this by using the overlapping region from the G141 observation (Figure 7, right-hand panel). For G141, SN 2019oyw's trace loses its signal strengths at long wavelengths, and we could extract meaningful information to about 16500 Å, where the contamination was still insignificant.

Figure 8 shows the reduced late-time spectra in the observing frame. The photometric data are also shown in the figure for flux comparison, which verifies a consistent calibration between the photometry and spectroscopy. This figure shows the declining flux density and narrowing of the spectral features

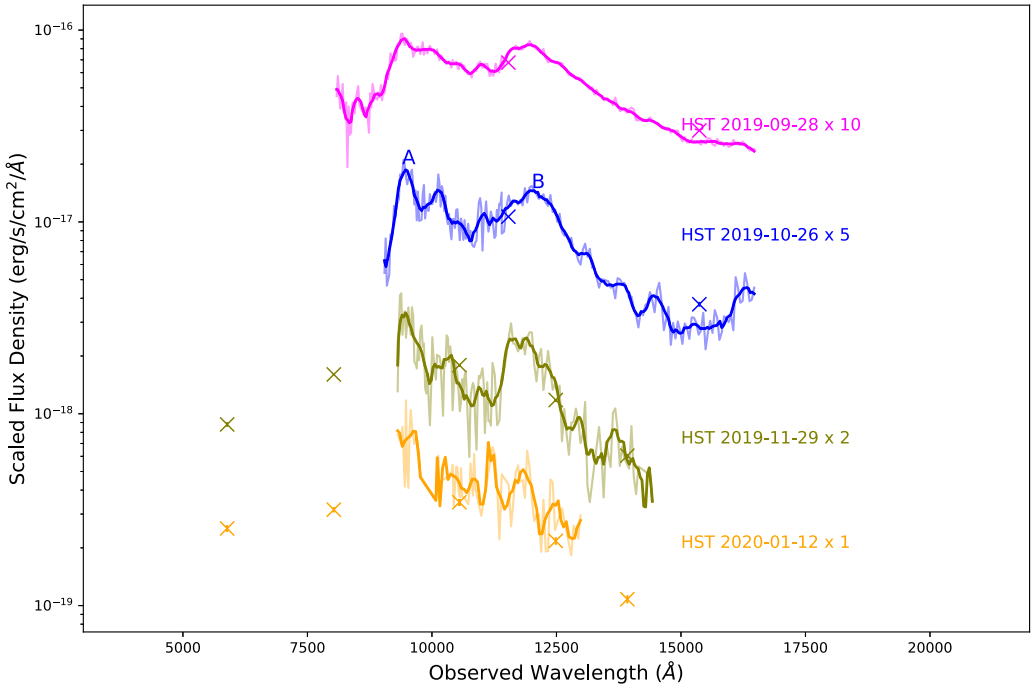

Figure 8. Spectral energy distribution of SN 2019oyw from several grism spectra taken between 2019 September 28 and 2020 January 12 using HST/WFC3. The plot shows raw spectra (faint lines) and their smoothed versions (solid lines). (We applied the generalized Savitzky–Golay method (R. M. Quimby et al. 2018) in smoothing the spectra. The resolution parameter was set to 60 (which is equivalent to the half width of 5000 km s^{-1}), and the polynomial order was set to $n = 2$, except the spectrum on 2020 January 12 using $n = 0$ because of low SNR.) Each spectrum was scaled vertically for visual clarity, and the corresponding scale factor is provided. The data points shown with crosses are the photometric observations (see Table 2) shown for comparison. "A" and "B" mark two prominent features (at about 9500 and 12000 Å, respectively) observed more clearly on 2019 October 26 spectrum. The observed flux densities are shown and are not corrected for the extinction.

with time. Note that we have cropped the three later spectra at the blue and red ends, compared to the 2019 September 26 spectrum (in magenta), due to the decrease in signal-to-noise ratio (SNR) as the source fades. Two prominent features are marked on the 2019 October 26 spectrum (in blue): "A" and "B" at about 9500 and 12000 Å, respectively. These features are visible starting 2019 September 28. Feature "B," although lower SNR, was also visible on 2019 November 19 (in green). The observed spectrum on 2020 January 12 (in yellow) has such low SNR that we cannot identify any feature.

2.3. VLT Spectroscopy

Additional to observations from the HST, K. Medler (2023) and Izzo et al. (2024, in preparation) provided us with their spectroscopic observations with the VLT for the analysis in this work. From K. Medler (2023), four epochs prior to the HST observations were observed by the VLT/FOcal Reducer and low dispersion Spectrograph (FORS; I. Appenzeller et al. 1998): 2019 September 2 (4 days after the trigger in observing frame), 2019 September 10 (12 days), 2019 September 15 (17 days), and 2019 September 20 (22 days). The VLT/FORS observations cover the wavelength range 3300–11000 Å. In Section 4, we combine this early VLT/FORS data with our later observations from HST to study the evolution with time of the Ca II NIR triplet $\lambda\lambda$8498, 8542, 8662 (see Section 4). Izzo et al. (2024, in preparation) used the VLT X-shooter (J. Vernet et al. 2011) to observe on 2021 September 11 and 2021 November 12. We were provided the 2D reduced spectrum (see Section 5) from the combined observations. These data reveal the spectrum of the environment at the location of the transient, which we use in our discussion in Section 5. A full discussion of these VLT data and their implications for the GRB 190829A/SN 2019oyw will be provided in Medler et al. (2024, in preparation) and Izzo et al. (2024, in preparation).

3. Offsets of Spectral Features and Redshift Re-estimation

We start our analysis by comparing the late-time HST spectra of SN 2019oyw with spectra of SN 1998bw (F. Patat et al. 2001), which has served as an archetype of GRB-SNe (Z. Cano et al. 2014; M. Modjaz et al. 2016). In Figure 9 upper panel, we show SN 2019oyw's spectrum at the epoch 2019 October 26 (the solid red line). This corresponds to a rest-frame phase of 53 days from the GRB trigger at $z = 0.0785$, the redshift of the SDSS galaxy. The letters "A" and "B" again mark the two prominent peaks at about 8700 and 11000 in rest frame, respectively. The black dashed line and the black solid line show spectra of SN 1998bw on 1998 June 12, or phase 47 days, and 1998 June 24, phase, 59 days, respectively. These two spectra, obtained from WISeREP (https://www.wiserep.org/; O. Yaron & A. Gal-Yam 2012), are combined here to cover a rest-frame wavelength range roughly equivalent to that observed using the G102 and G141 grisms on SN 2019oyw. Black vertical lines mark the rest wavelengths of the emission line of CaIR3 (for the Ca II NIR triplet $\lambda\lambda$8498, 8542, 8662) and He I (for the He I λ10830).

Immediately, one notices that the features of the two transients appear offset. To better understand this issue, we experimented by assuming different redshifts for SN 2019oyw, and found an approximate redshift of $z = 0.1$. We improved upon this using cross correlation (see Appendix for details) arriving at a best estimate of $z^* = 0.1051$. (We will discuss the errors of this estimate later, when we further discuss the time evolution of the CaIR3 peak in the following section). In Figure 9 lower panel, the redshift z^* is instead assumed for SN 2019oyw (in blue solid line). Assuming z^* shows better

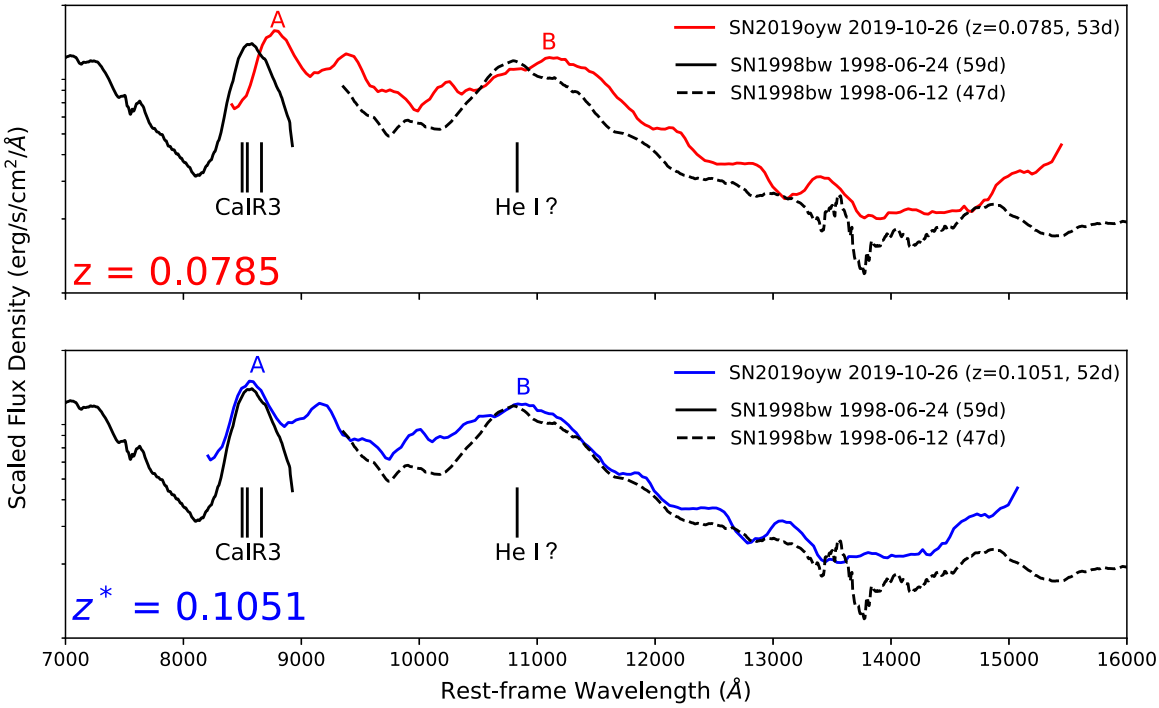

Figure 9. Alignment of SN 2019oyw's late-time spectral features. Both panels show rest-frame wavelength on the x-axis, and on the y-axis the flux densities which are scaled for visual clarity. Upper panel: Redshift $z = 0.0785$ is assumed for SN 2019oyw on epoch 2019 October 26 (red, phase 53 days) as the source. The letters "A" and "B" mark two prominent peaks in the spectrum. Spectra of both objects were extinction corrected. SN 1998bw is chosen as the standard GRB-SN template (Z. Cano et al. 2014; M. Modjaz et al. 2016). Epochs 1998 June 12 (black dashed line, 47 days) and 1998 June 24 (black solid line, 59 days) cover rest-frame wavelengths comparable to our observations in G102 and G141 grisms, and are comparable in phase to our observations of SN 2019oyw. The Ca II NIR triplet $\lambda\lambda$8498, 8542, 8662 (CaIR3) and He I λ10830 are markers close to A and B, respectively. For SN 2019oyw, we adopted values $E(B-V) = 0.049$, 0.757 for Galactic (E. F. Schlafly & D. P. Finkbeiner 2011; Y. D. Hu et al. 2021) and extragalactic (Milky Way model) reddening (L.-L. Zhang et al. 2021), respectively. For SN 1998bw, we adopted $E(B-V) = 0.059$ and its host's $A_V = 0.17$ assuming Small Magellanic Cloud dust model (see L. Li et al. 2018 and references therein). Lower panel: Similar to the upper panel but assuming $z^* = 0.1051$ for SN 2019oyw instead (blue, phase 52 days). By comparing between the two cases, it is evident that assuming z^* improves the alignment.

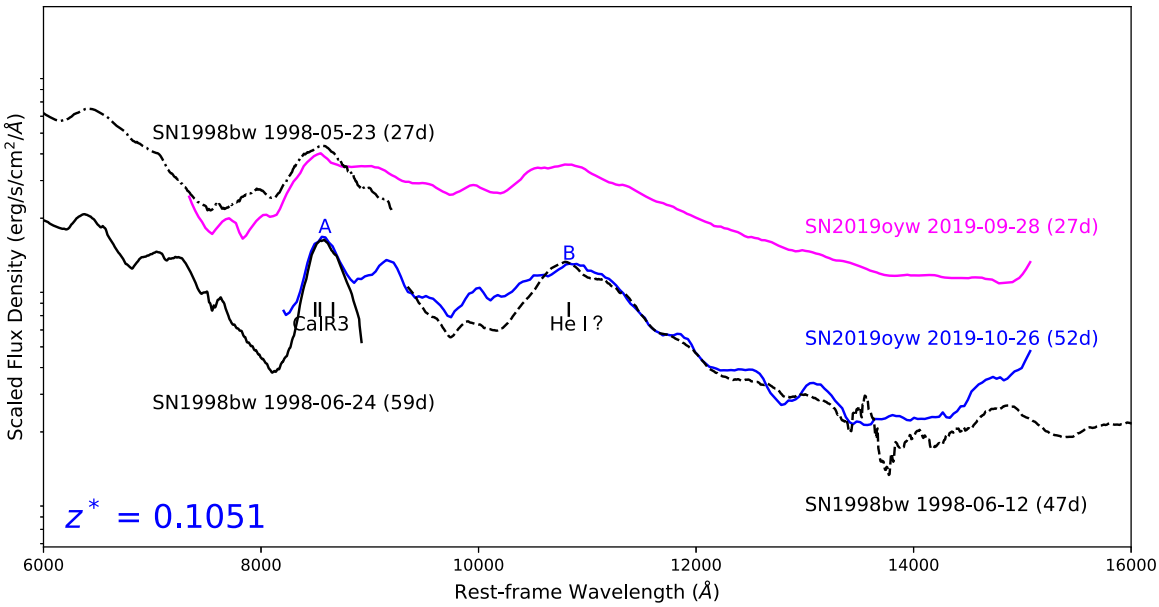

Figure 10. Alignment of SN 2019oyw's late-time spectral features assuming $z^* = 0.1051$. The figure shows rest-frame wavelength on the x-axis, and on the y-axis the flux densities which are scaled for visual clarity. Spectra on epochs 2019 September 28 (magenta, 26 days) and 2019 October 26 (blue, 52 days) are shown (omitting epochs 2019 November 29 and 2020 January 12 spectra due to low signals). Spectra of SN 1998bw at similar phases are shown for comparisons. These spectra were extinction corrected. The figure supports consistency of the feature alignment assuming z^*.

feature alignment across the *entire* spectrum. This implies that the feature "A" agrees well with the wavelength of the CaIR3 complex, and feature "B" with He I; however, as described in the discussion (Section 6), there are good reasons to believe that elements other than He may be responsible for this feature.

We build upon this in Figure 10 by including the spectrum from the epoch 2019 September 28. At the redshift of

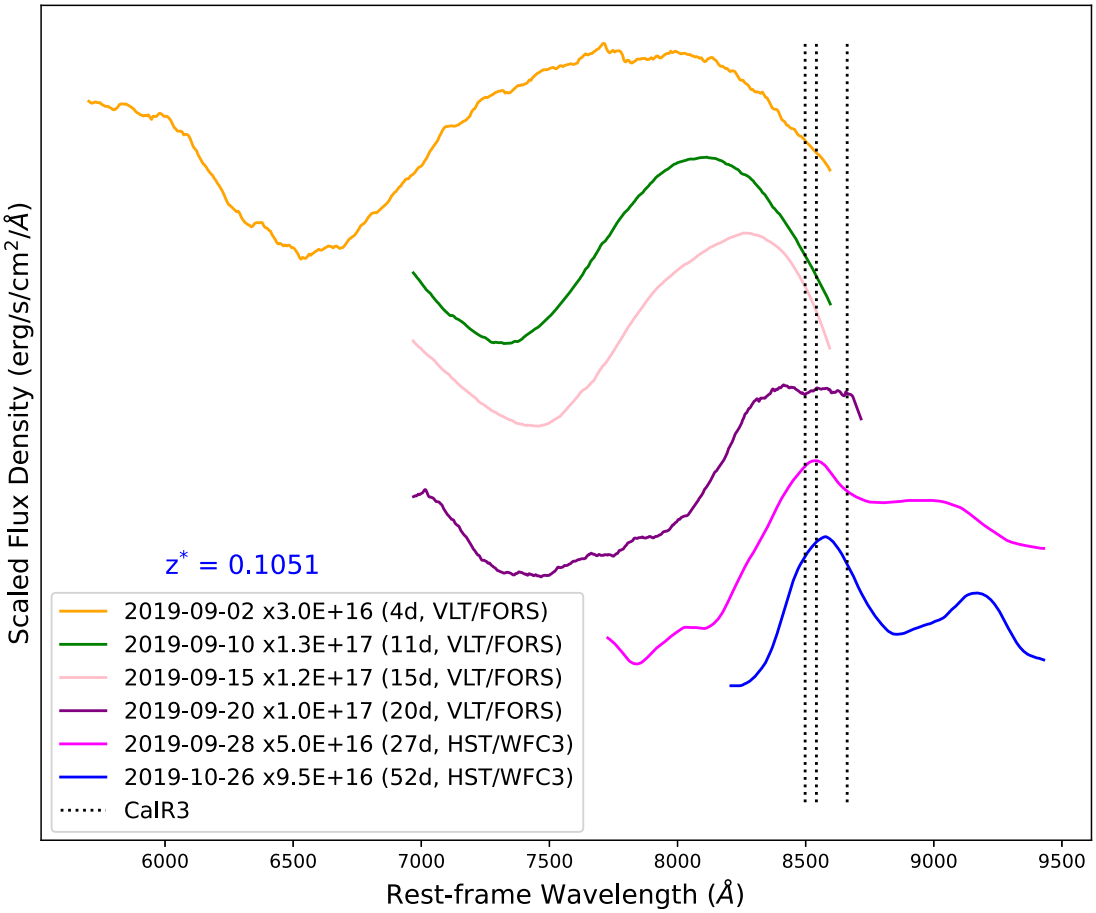

Figure 11. Evolution of SN 2019oyw's CaIR3 feature. The spectra in this plot show the evolution of the CaIR3 feature from 4 days after burst to 52 days after burst (in rest frame, assuming $z^* = 0.1051$). The spectra are scaled for legibility and do not represent the evolution of the spectral flux; the scaling factors are provided in the legend. The peak evolves from the blue back toward the rest-frame wavelengths of the CaIR3 interval as the expansion of the photosphere slows. As we will discuss, this is a common feature of Type Ic and Ic-BL supernovae, and understanding this time evolution is critical for accurately estimating the true redshift of SN 20190yw. These spectra are extinction corrected and smoothed (see Section 2.2 for details).

$z^* = 0.1051$, this is equivalent to phase 27 days. The spectrum of SN 2019oyw (in pink solid line) is shown against SN 1998bw on 1998 May 23 (in black dotted–dashed line) which also is at phase 27 days. We repeat the epochs from ∼50 days in this figure to better allow comparison. The plot shows consistent alignment of SN 2019oyw's prominent feature "A" in both epochs, again assuming $z^* = 0.1051$. (SN 1998bw's spectrum at the earlier epoch does not extend sufficiently in the red to check the alignment of feature "B".) However, the alignment of both epochs strongly supports the contention that SN 2019oyw has an apparent redshift that is significantly greater than that of the large spiral on which it is superposed.

4. Evolution of Calcium II NIR Triplet During Late-photospheric Phase in Supernovae Type Ic-BL and Ic

We showed in the previous section that by assuming $z^* = 0.1051$, instead of $z = 0.0785$, the late-time spectral features of SN 2019oyw can be much better aligned with templates from SN 1998bw. The cross correlation we used for fine-tuning the redshift works by aligning the CaIR3 peaks of the source and the template (see Appendix). However, as we will discuss in this section, this feature and its peak wavelength will change over time as the expanding photosphere slows. Here, we investigate the time evolution of the CaIR3 feature and compare SN 2019oyw with samples of SNe Ic-BL and Ic.

Figure 11 shows the time evolution of CaIR3 observed on SN 2019oyw's spectra from 2019 September 2 to 2019 October 26. Prior to three weeks after the explosion we use, with permission, VLT/FORS spectra from K. Medler (2023; see also Section 2.3). Later spectra are the HST observations presented above. The CaIR3 feature displays a characteristic P-Cygni profile. This implies the supernova is in its photospheric phase (S. A. Sim 2017) throughout. We note that for a supernova the transition between photospheric and nebular phases is typically about 100 days after explosion (S. J. Prentice et al. 2022). The feature and its peak are clearly seen to migrate from blue to red with time.

Figure 12 shows the time evolution of CaIR3 features of SN 1998bw (F. Patat et al. 2001). The CaIR3 feature of this archetypal GRB-SN evolved in a very similar fashion. For comparison, we also plot SN 2019oyw's CaIR3 feature from epochs 2019 September 28 (26 days) and 2019 October 26 (52 days) assuming $z^* = 0.1051$ in the figure along with the SN 1998bw data. The alignment of these two SNe supports the matching of the evolution of the P-Cygni profiles of CaIR3 if z^* is assumed.

With both GRB-SNe 1998bw and 2019oyw showing similar evolution of the CaIR3 feature during the photospheric phase,

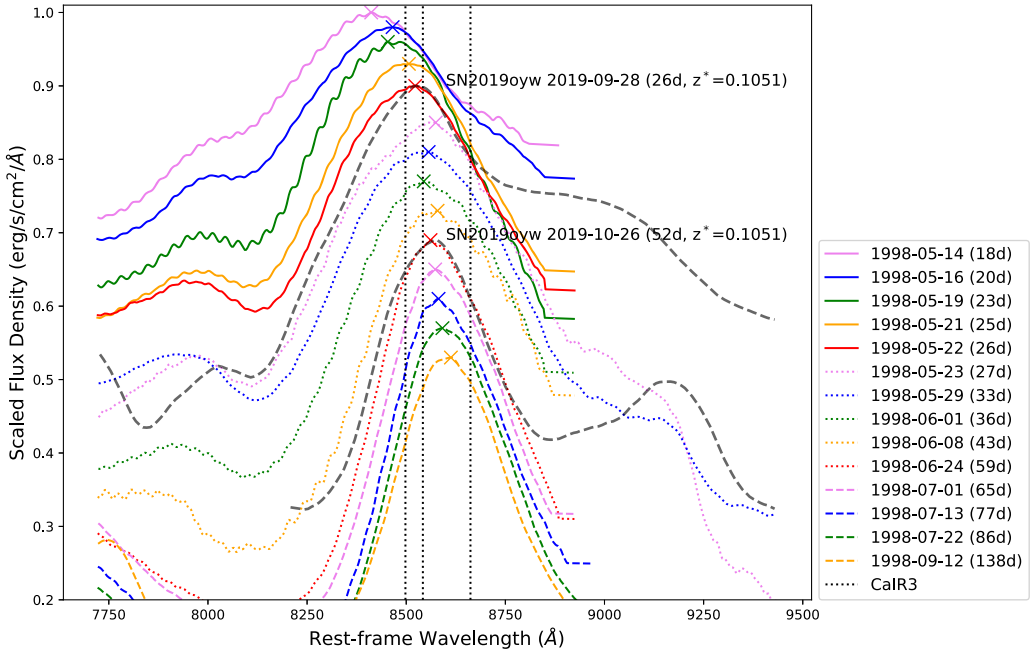

Figure 12. Evolution of SN 1998bw's CaIR3 emission. This figure shows rest-frame wavelengths on x-axis and flux densities on y-axis are scaled for visual clarity. SN 1998bw's spectra from 1998 May 14 (18 days) to 1998 September 12 (138 days) are shown in order from top to bottom by epoch (F. Patat et al. 2001). This figure features peaks of CaIR3 (marked by crosses). The evolution shows that the peaks become redder with age. They started to be inside the constraint starting at phase 25 days and stayed inside the constraint until at least 138 days. We discuss more about the evolution in Section 4. Spectra of SN 2019oyw on epochs 2019 September 28 and 2019 October 26 (black dotted lines) are also shown in the figure (assuming $z^* = 0.1051$) for comparisons with SN 1998bw at similar phases. These spectra were smoothed by the generalized Savitsky–Golay method (R. M. Quimby et al. 2018; see Section 2.2 for details) and extinction corrected. We also note that the small oscillation (also known as "fringing") observed on some of SN 1998bw's spectra (e.g., 18 and 23 days) is the feature seen in the original data, and is not an artifact from our process.

we further investigate this commonality by showing the evolution of the CaIR3 peak emission in a larger sample of Type Ic-BL SNe in Figure 13. The sample includes SNe both with and without associated GRB. (See M. Modjaz et al. 2016 and references therein for further references of these objects.) This figure shows the rest-frame wavelength of the evolving CaIR3 peak (in each object's rest frame) on the x-axis and the associated phases on y-axis. SN 2019oyw's CaIR3 peak is shown in the figure in blue (assuming $z^* = 0.1051$) and red (assuming $z = 0.0785$). In the figure, we observe a similar evolution of CaIR3 peaks migrating from blue toward red with age. This figure shows that the apparent peaks at early phases can be bluer than 8498 Å, the bluest of the CaIR3 lines. However, the evolution eventually brings the peaks back to be consistent with the CaIR3 interval during late-photospheric phase. Most objects show their CaIR3 peaks residing inside the rest-frame CaIR3 wavelength range starting from 30 to 100 days. An exception is GRB-SN 2010bh, which possessed significantly higher expansion velocity than the standard GRB-SN 1998bw at similar phases (R. Chornock et al. 2010; F. Bufano et al. 2012).

Similarly, Figure 14 shows the evolution of CaIR3 peaks from a sample of SNe Ic (square data points; see also M. Modjaz et al. 2016 and references therein). We note that for a SN without GRB, which is the case for all these SNe Ic, phase is referred from the date of discovery. The data for these transients were downloaded from WISeREP (https://www.wiserep.org/; O. Yaron & A. Gal-Yam 2012), and we verified other relevant information such as the date of discovery and redshift from the Transient Name Server (https://www.wis-tns.org/). Like SNe Ic-BL, their CaIR3 peaks evolve to be redder with time; unlike SNe Ic-BL, most of the SNe Ic do not exhibit a CaIR3 peak bluer than the CaIR3 interval, due to their smaller expansion velocities. Shown among the sample, PTF 12gzk is an example of Type Ic that behaved more similarly to the Type Ic-BL by exhibiting a bluer peak than the interval at early photospheric phase with a rapid motion to redder wavelengths, it then transitioned to a slow motion once the peak already resided within the interval. We note that PTF 12gzk was an unusual Type Ic exhibiting fast ejecta expansion velocities similar to Type Ic-BL but not persistent broad lines (S. Ben-Ami et al. 2012).

We observe from the SNe Ic sample that their CaIR3 peaks slowly become redder while residing inside the CaIR3 interval through the late-photospheric phase until about 100 days, similar to the Ic-BL sample. Beyond this, moving into the nebular phase some objects show CaIR3 peaks redder than 8662 Å, which may be explained by contributions from [C I] λ8727 and Fe II λ8830 (S. J. Prentice et al. 2022).

From these samples, we note three key observations:

1. For each object, the peak of the CaIR3 evolves from blue to red with time, with this evolution being particularly rapid at early epochs when the peak is observed to be bluer than the bluest line in the triplet, i.e., 8498 Å.
2. However, the CaIR3 peak evolves more slowly inside the interval, i.e., $8498 \leqslant \lambda_{\rm CaIR3} \leqslant 8662$ Å.
3. The peaks are well constrained within the CaIR3 interval at late-photospheric phase (typically after 30 days) because the curve turns nearly vertical at this phase.

In Figures 13 and 14, SN 2019oyw is displayed assuming both $z = 0.0785$ (red) and $z^* = 0.1051$ (blue). The data show the evolution of the CaIR3 peak of SN 2019oyw follows a typical path if z^* is assumed. However, if $z = 0.0785$ is

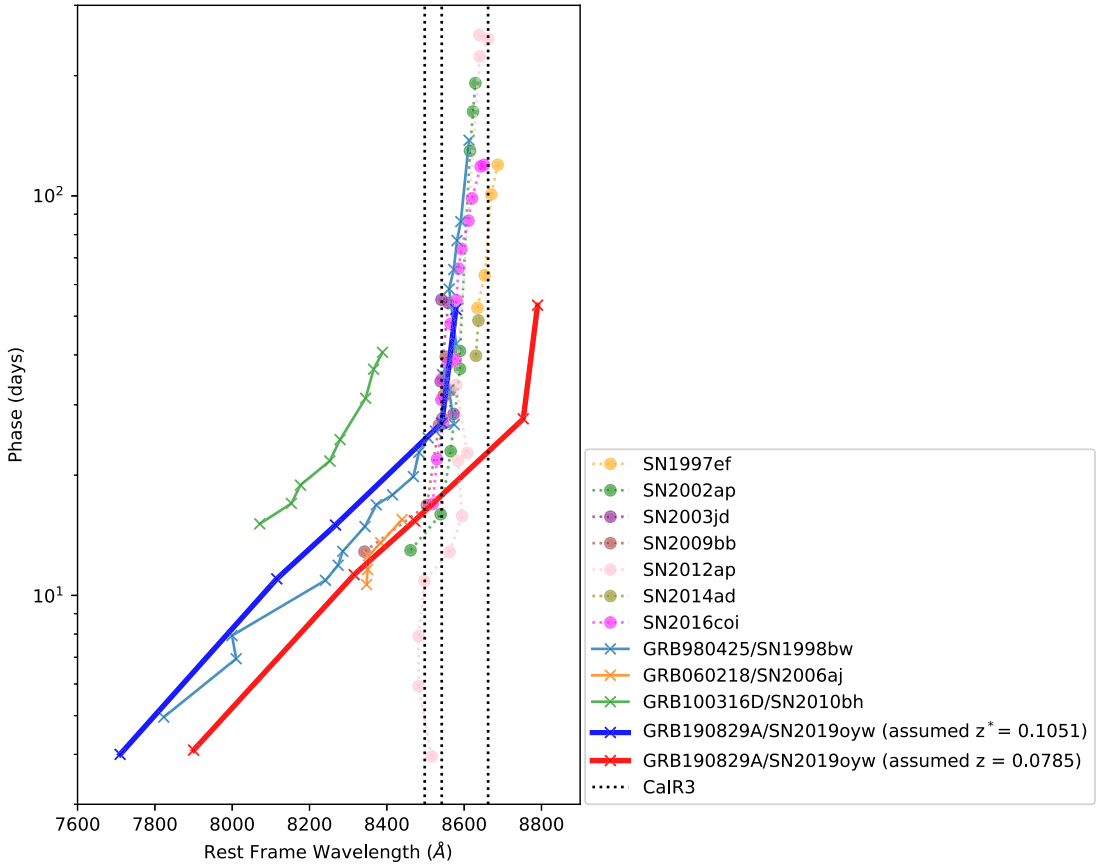

Figure 13. Evolution of CaIR3 peaks from samples of SNe Ic-BL. Rest-frame wavelengths are shown on the x-axis and phases are on the y-axis. The samples include SNe Ic-BL with associated GRBs (cross data points), and without GRB (dot data points). Phase is referred from the GRB trigger. The samples show the evolution of CaIR3 peaks from blue to red with ages, and the peaks are well constrained within the CaIR3 constraint if considering late-photospheric phases between 30 and 100 days; see Section 4 for more discussion. SN 2019oyw's CaIR3 peaks are also shown in red (assuming $z = 0.0785$) and blue (assuming $z^* = 0.1051$). We noted that early data of SN 2019oyw from VLT/FORS (see Section 2.3). The plot shows that assuming $z^* = 0.1051$ improves the feature alignment better than $z = 0.0785$.

assumed, the CaIR3 peak of SN 2019oyw is significantly redder than any other SN in the sample, and at late times the observed spectral peak would have to somehow be transferred to another set of line or lines redder than the CaIR3 triplet. The primary suspect for these lines would be [C I] λ8727 and Fe II λ8830, which tends to appear in the nebular phase (S. J. Prentice et al. 2022). Therefore, we think this explanation is unlikely.

Given the samples, the uncertainties from our cross correlation result of z^* (see Appendix) are dominated by two important choices we made, rather than the statistics from the cross correlation technique itself. First, we chose the epoch 2019 October 26 for the cross correlation because this is clearly already on the slow-motion part of the CaIR3 peak's evolution, which we think began around the epoch 2019 September 28. Assuming that the epoch 2019 October 26 is on the slow-motion part, to behave like the other SNe in the sample, the peak wavelength must reside inside the CaIR3 interval. However, where exactly the peak should be inside the interval depends on the choice of the template. Therefore, a conservative method to estimate the redshift uncertainty is to ask what redshift is required to move the CaIR3 peak on 2019 October 26 inside the CaIR3 interval, i.e., 8498–8662 Å. This redshift range is $0.0944 \leqslant z^* \leqslant 0.1156$, and we use this interval as our final estimate of z^*. We note that this estimate is derived from the samples of SNe Ic-BL and Ic presented above, not only from the SN 1998bw.

5. Physical Scenarios

The result of redshift $z^* = 0.1051$ showing best alignment challenges our understanding of this event. GRB 190829A/SN 2019oyw superposed on the galaxy SDSS J025810.28–085719.2, and that galaxy's gas imposed absorption lines detected in the early afterglow (Y. D. Hu et al. 2021). Therefore, assigning this galaxy as the host and adopting redshift $z = 0.0785$ was intuitive. However, if this was correct, the evidence presented here would imply that SN 2019oyw is a very unusual object.

If the SN 2019oyw is actually in a host at a redshift of $z = 0.0785$, the observed CaIR3 peak of SN 2019oyw corresponds to a peculiar velocity with respect to the galaxy of $\sim$4000 km s^{-1} in the radial direction away from the observer. Physically, this might be explained by an apparent asymmetry in the SN expansion such that line-emitting materials with high velocities away from us were dominating the observations. However, this implies that what we are seeing is dominated by light from the far side. Considering that the light from the far side should be more attenuated and obscured due to the intervening material on the closer side, how this scenario can explain the observation is uncertain.

Another possible explanation is that the explosion occurred in a progenitor with an exceptionally high proper velocity. In a three-body interaction (W. R. Brown 2015), a binary (each with $3\,M_\odot$, with semimajor axis of the binary 0.5 au) interacting with a massive black hole ($\sim 10^6\,M_\odot$) can disrupt one of the binaries and eject the other with final velocity at

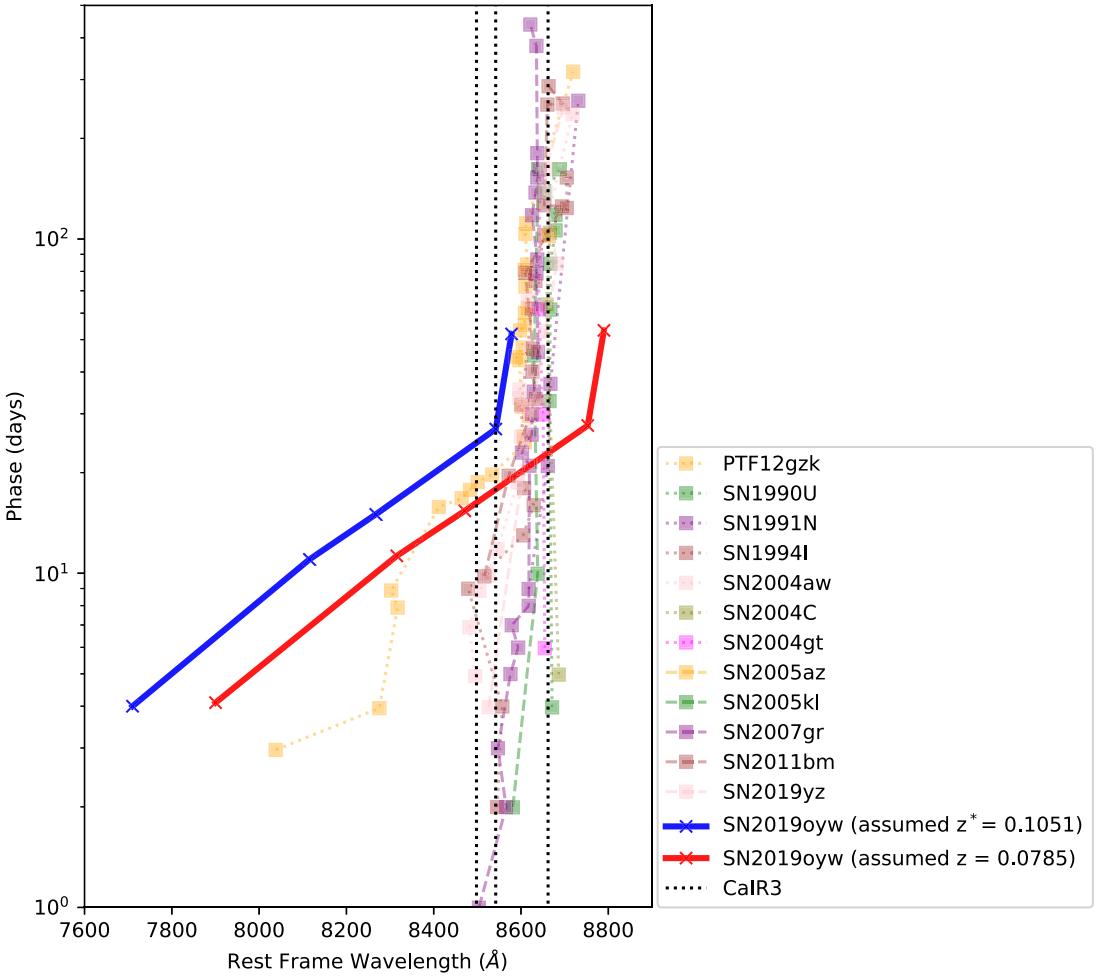

Figure 14. Similar to Figure 13 but with a sample of SNe Ic (square data points) instead. We note that phase is referred from the date of discovery for these SNe without associated GRB.

infinite distance of the order of 1000 km s^{-1}. We note that the estimated ejected velocity increases with the mass of the black hole M and the mass of the binary system, m_b as $M^{1/6}m_b^{1/3}$. For this event, the progenitor of GRB 190829A was a massive star (i.e., $\gtrsim$20 $M_\odot$ at zero-age main sequence; A. Levan et al. 2016). The SDSS galaxy has nuclear emission line ratios (Izzo et al. 2024, in preparation and Patricia Schady via personal communication), which imply the presence of an AGN, which therefore implies a supermassive black hole that is likely more massive than 10^7 $M_\odot$ (J.-H. Woo & C. M. Urry 2002).

However, the progenitor need not have an exceptional proper motion with respect to its host galaxy, if in actuality it was in a dwarf galaxy situated behind the apparent SDSS galaxy. We note that recent studies show evidence such as very high stellar mass (R. Gupta et al. 2022) and the presence of AGN supporting that if the SDSS galaxy is the host of the long GRB 190829A, it would be atypical for a long GRB host (D. A. Perley et al. 2016).

In Figure 4, we show the location of the burst the template images taken from HST/WFC3 during 2021 January (i.e., about 500 days after the burst in the observing frame). In these images, SN 2019oyw had faded below the detection levels of the telescope. The red circle in each image shows an aperture of 0.″39 in radius centered on the supernova, using the last detection as a reference. In the vicinity of the burst's location, we observed a dust lane extending from north to south on the west. We note a bright clump at the western edge of the red circle in the F125W and F140W NIR images. However, the template images do not show clear evidence of any dwarf galaxy behind the SDSS galaxy at the burst's location.

In Figure 15, we show the 2D spectrum taken from X-shooter (Izzo et al. 2024, in preparation). The spectrum shows emission lines including Hα, [N II], and [S II] corresponding to the SDSS galaxy at $z = 0.0785$. These are marked in red. The expected locations of the same set of lines assuming $z^* = 0.1051$ are marked in blue. We note that these lines are strong emission lines typically observed in star-forming galaxies (L. J. Kewley & S. L. Ellison 2008), which are the preferred hosts of GRB-SN events (A. S. Fruchter et al. 2006; M. Modjaz et al. 2020). As can be seen in Figure 15, the spectrum reveals no clear sign of a more distant galaxy.

The nondetection does not completely reject the possibility of an existing dwarf galaxy at $z^* = 0.1051$ because it could be hidden behind the bright and dusty foreground SDSS galaxy (R. Gupta et al. 2022). From the 2D spectrum, we can place an upper limit if there was a point source, such as a bright H II region, emitting Hα from $z^* = 0.1051$. The estimated root mean square of the sky region around 7253 Å (i.e., Hα at z^*) is 3.37×10^{-19} erg s^{-1} cm^{-2} Å^{-1} in a pixel. This is equivalent to

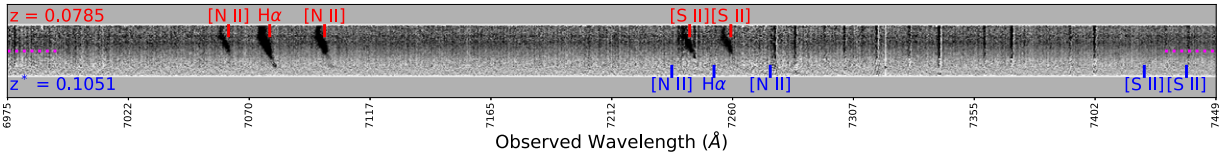

Figure 15. Two-dimensional spectrum at the location of GRB 190829A/SN 2019oyw taken by X-shooter. The location of the transient was placed at the center of the slit (horizontal magenta dotted lines). *X*-axis is shown in observed wavelengths. The spectrum is shown in the middle, and line markers are shown at the top for assuming $z = 0.0785$ (red) and bottom for $z^* = 0.1051$ (blue). These markers include Hα λ6563, [N II] $\lambda\lambda$6548, 6583, and [S II] $\lambda\lambda$6717, 6731. The image is shown in inverse color, i.e., black = bright. The observed lines are consistent with the SDSS J025810.28–085719.2 at the redshift $z = 0.0785$. See more details about this observation in Izzo et al. (2024, in preparation).

the observing upper limit about 6.88×10^{-18} erg s^{-1} cm^{-2} in the integrated flux assuming a point source.[18]

We note that in this scenario the Hα emission from $z^* = 0.1051$ passes through the SDSS foreground galaxy at $z = 0.0785$ before being observed by the telescope. Since the attenuation of the Hα emission is mostly due to the SDSS galaxy, the dilated wavelength of the Hα emission arriving at the SDSS galaxy would be redshifted by about $z' \approx 0.0247$ (i.e., shifted to $\sim$6725 Å). By assuming $A_V = 2.33$ estimated from the afterglow (L.-L. Zhang et al. 2021), the extinction factor is $\sim$0.18. This implies the extinction-corrected upper limit 3.82×10^{-17} erg s^{-1} cm^{-2}. This is equivalent to 1.08×10^{39} erg s^{-1} (luminosity distance to $z^* = 0.1051$ is 487 Mpc). By comparing this upper limit to the H II region luminosity function observed from 19 nearby spiral galaxies (F. Santoro et al. 2022), this upper limit is at the percentile between 86th to 99th (with average 94th). This implies that about 90% of these regions would be undetected considering the current upper limit.

It is perhaps interesting to ask what we would see if GRB 190829A/SN 2019oyw had gone off on a host like that of GRB 980425/SN 1998bw. The HST has an angular resolution approximately 10 times better than ground-based imaging. Therefore, HST imaging of the host of GRB 190829A/SN 2019oyw has roughly the same physical resolution as ground-based imaging of the host of GRB 980425/SN 1998bw, ESO 184-G82, at $z = 0.0085$, whose H II regions were studied by L. Christensen et al. (2008). If we assume the missing distant galaxy at $z^* = 0.1051$ to be similar to the SN 1998bw's host, we can compare the estimated upper limit. This study found Hα strengths of the H II regions spanning from about $\sim 10^{37}$ to 10^{39} erg s^{-1}. All but one of these roughly two-dozen H II regions would be $\lesssim 1\sigma$ sources in our observations were they in the hypothesized dwarf host of SN 2019oyw. Thus, to find no such source would not be too surprising.

Finally, we note that if SN 2019oyw occurred at $z^* \sim 0.1$ rather than $z = 0.785$ its *r*-band absolute magnitude would be about 0.5 mag brighter than SN 1998bw instead of matching it closely (K. Medler 2023). However, some SNe Ic-BL, both with (S. Schulze et al. 2014; V. L. Toy et al. 2016; G. P. Srinivasaragavan et al. 2024) and without (F. Taddia et al. 2019) a known GRB association, have been this bright. Furthermore, K. Medler (2023) finds that when SN 2019oyw is assumed to be at the redshift of the large $z = 0.0785$ spiral, its pseudobolometric luminosity is somewhat less than that of SN 1998bw; however, we calculate that if instead it were at $z^* = 0.1051$, its pseudobolometric luminosity would agree with that of SN 1998bw to within a couple of percents. Thus, the luminosity of the SN does not cause us to strongly prefer one distance solution over the other.

6. Discussion and Summary

GRB 190829A/SN 2019oyw was observed between 2019 September 28 and 2021 January 9 using the HST/WFC3. Images and spectra of the transient showed a clear sign of the fading SN 2019oyw in both optical and NIR. Its late-time light curve faded with the decay rate consistent with Co^{56} powering mechanism (Figure 5), typical for late-time GRB-SNe (S. E. Woosley & A. Heger 2006) until the last detection on 2020 February 16. The spectra (Figure 8) showed broad P-Cygni profiles which narrowed and deblended with time. In particular, two prominent peaks, marked as "A" and "B" in figures, were clearly visible. We attempted to identify the features by aligning the spectra against that of the standard GRB-SN 1998bw. However, we found that the spectral features were redshifted by about 4000 km s^{-1} from the redshift of the large foreground SDSS spiral whose absorption features are observed in the afterglow spectra of GRB 190829A, $z = 0.0785$. This velocity offset can be best measured using the Ca II NIR triplet $\lambda\lambda$8498, 8542, 8662 (CaIR3) emission, but is also seen near the He I λ10830 feature and the overall shape of the NIR spectrum (see Figure 9). This widespread shift makes the idea that we are seeing an unusual blending of lines appear unlikely.

To better understand the behavior of the spectra, we analyzed the CaIR3 evolution in a large sample of Type Ic-BL and Ic SNe from the literature (Figures 13 and 14, respectively). From the samples, we highlighted key observations (see Section 4). The samples show that a CaIR3 peak evolve from blue to red with time, with this evolution being particularly rapid at early photospheric phases when the peak is observed to be bluer than the bluest line in the triplet (i.e., 8498 Å). Inside the interval (i.e., 8498–8662 Å), the peak evolves more slowly, as the curve turns nearly vertical. The CaIR3 peaks are well constrained within the interval during late-photospheric phases starting at about 30 days. The comparison to the samples showed no other object with the CaIR3 line as red as that of SN 2019oyw were it truly at the redshift of the SDSS galaxy. Assuming instead that SN 2019oyw behaved similarly to the SNe in the samples, we re-estimated the redshift to be $0.0944 \leqslant z^* \leqslant 0.1156$. With this new alignment, we confidently identified the feature "A" as the Ca II NIR triplet $\lambda\lambda$8498, 8542, 8662. In contrast, we cannot be certain which spectral features are associated with feature "B." Without the detection of other He I lines such as He I 2.058 μm we cannot confirm the association of feature "B"

[18] For this observation from X-shooter (more details in Izzo et al. 2024, in preparation), the wavelength dispersion (*x*-axis) is 2 Å pix^{-1} with 5.7 pix/FWHM (full width at half-maximum; J. Vernet et al. 2011). We assumed a point-spread function of 0.″7 /FWHM (F. Schönebeck et al. 2014), which is equivalent to 4.375 pixels/FWHM given 0.″16 pixel^{-1} in the cross-dispersion direction (*y*-axis).

with He I rather than other features such as Mg II (L. B. Lucy 1991; P. A. Mazzali & L. B. Lucy 1998; F. Patat et al. 2001; S. Taubenberger et al. 2006; R. Chornock et al. 2010; F. Bufano et al. 2012; L. Izzo et al. 2019).

Since GRB 190829A/SN 2019oyw is superposed on the galaxy SDSS J025810.28–085719.2 whose gas was seen in Ca II H/K absorption in the early afterglow, assigning this galaxy as the host was intuitive. However, our surprising result challenges this picture. If the SDSS galaxy is its actual host, the evidence implies that SN 2019oyw was very unusual. The redshifted features offset by 4000 km s^{-1} could be a consequence from an observing asymmetry such that the line-emitting materials from the far side (i.e., moving away from observers) were dominating the observations. It is far from obvious how one gets the dominance of the far side. Another possible explanation (see Section 5) involves a progenitor with high velocity, such as one that would be produced by a three-body interaction of a tight and massive binary and a supermassive black hole (W. R. Brown 2015). We note that the presence of an AGN was observed in the SDSS galaxy (Izzo et al. 2024, in preparation and Patricia Schady via personal communication), which implies the presence of a supermassive black hole likely more massive than $10^7\,M_\odot$ (J.-H. Woo & C. M. Urry 2002).

Instead, if we placed the explosion further behind the SDSS galaxy on a smaller dwarf galaxy at z^*, the observed discrepancies could be straightforwardly resolved. In this scenario, the spectral features of SN 2019oyw evolved similarly to other SNe Ic-BL and Ic in the comparison samples. Given that the SDSS galaxy is bright and dusty, especially at the location of the event, searching for a more distant dwarf host would be challenging. The available images from HST and the spectra from the X-shooter show no sign of such a system. We note that these observations were not designed to see beyond the foreground SDSS galaxy, and were done before we knew about this surprising evidence. We estimate the upper limit of the Hα emission from a bright H II region in a background galaxy at z^*, and show that our nondetection does not by any means rule out the presence of such a host. We encourage further investigation with a design that can overcome observing challenges and see beyond the bright and dusty SDSS galaxy, such as a radio search for H I emission from the potential dwarf host.

In summary, we present a surprising result on the origins of the nearby GRB 190829A. Our story is similar to GRB 020819B (D. A. Perley et al. 2017) and GRB 130702A (P. L. Kelly et al. 2013) in that there is new evidence supporting a possible revision of the assigned host of the event. The possible need for such a revision is not a total surprise given that several studies had already pointed out that the SDSS galaxy is quite atypical for a long-duration GRB host. In particular, the SDSS galaxy was estimated to have stellar mass on the order of $10^{12}\,M_\odot$ (R. Gupta et al. 2022), which is very massive for a long GRB host. There is also evidence indicating the presence of AGN from the galaxy, which is atypical for a long GRB host. However, if the explosion was behind the foreground spiral, GRB 190829A/SN 2019oyw could be one among the typical cases like GRB 980425/SN 1998bw (T. J. Galama et al. 1998).

Finally, the work here provided insights into the time evolution of GRB-SNe and a potential method for directly determining the redshift of a GRB-SN. We demonstrated in Section 4 that using the CaIR3 feature has advantages due to the strong signal strength, stability, and slow evolution during late-photospheric phase from phase about 30–100 days. The accuracy of this method is of the order of 1000 km s^{-1}. We encourage further studies of the use of CaIR3 for the redshift estimation. In contrast to other existing methods (M. Li et al. 2023), this method allows us to estimate the redshift of the explosion using the lines of the associated supernova. Furthermore, since CaIR3 is a common feature typically observed in a supernova regardless of its class (G. H. Marion et al. 2009; D. R. van Rossum 2012; Z. Cano et al. 2014; J. M. Silverman et al. 2015; M. Modjaz et al. 2016; C. P. Gutiérrez et al. 2017; S. J. Prentice et al. 2022), the use of CaIR3 for redshift estimation could benefit not only the cases of GRB-SNs but also potentially other calcium-rich transients.

Acknowledgments

This research is based on observations made with NASA/ESA Hubble Space Telescope obtained from the Space Telescope Science Institute, which is operated by the Association of Universities for Research in Astronomy, Inc., under NASA contract NAS 5-26555. The HST observations presented here were taken under General Observer(GO) Programs 15089, 15510, 16042, and 16320. Support for K.B. was provided through grants associated with GO Programs 15510, 16042, and 16320 from the STScI under NASA contract NAS5-26555.

This research made use of Photutils, an Astropy package for detection and photometry of astronomical sources.

This work made use of the data products generated by the Modjaz group (formerly NYU SN group), and released under doi:10.5281/zenodo.58766 (Y.-Q. Liu et al. 2016), available at https://github.com/nyusngroup/SESNtemple/.

K.B. thanks Dr. Robert Quimby for sharing code that performs the generalized Savitzky–Golay method (R. M. Quimby et al. 2018).

S.B. acknowledge support from the PRIN-INAF 2022 project "Shedding light on the nature of gap transients: from the observations to the model."

This project was conducted during the pandemic of COVID-19. We would like to thank every individual both inside and outside the scientific communities for all their efforts during this hard time. We would also like to offer our deepest and most sincere condolences for every loss.

Appendix
Using Cross Correlation to Determine Redshift of SN 2019oyw

In this section, we present our use of cross correlation (S. Blondin & J. L. Tonry 2007) to estimate the redshift of SN 2019oyw. Our aim was to perform the cross correlation around the CaIR3 emission of SN 1998bw and the feature "A" of SN 2019oyw as shown in Figures 9 and 10. The epoch 2019 October 26 was chosen for the computation to limit the complication from line blending because the feature is relatively narrow and high SNR at this epoch. The epoch 1998 June 24 of SN 1998bw (F. Patat et al. 2001), which is at a comparable phase, was chosen as the GRB-SN template (Z. Cano et al. 2014; M. Modjaz et al. 2016).

We implemented our code to perform the cross correlation following S. Blondin & J. L. Tonry (2007), except that we did a

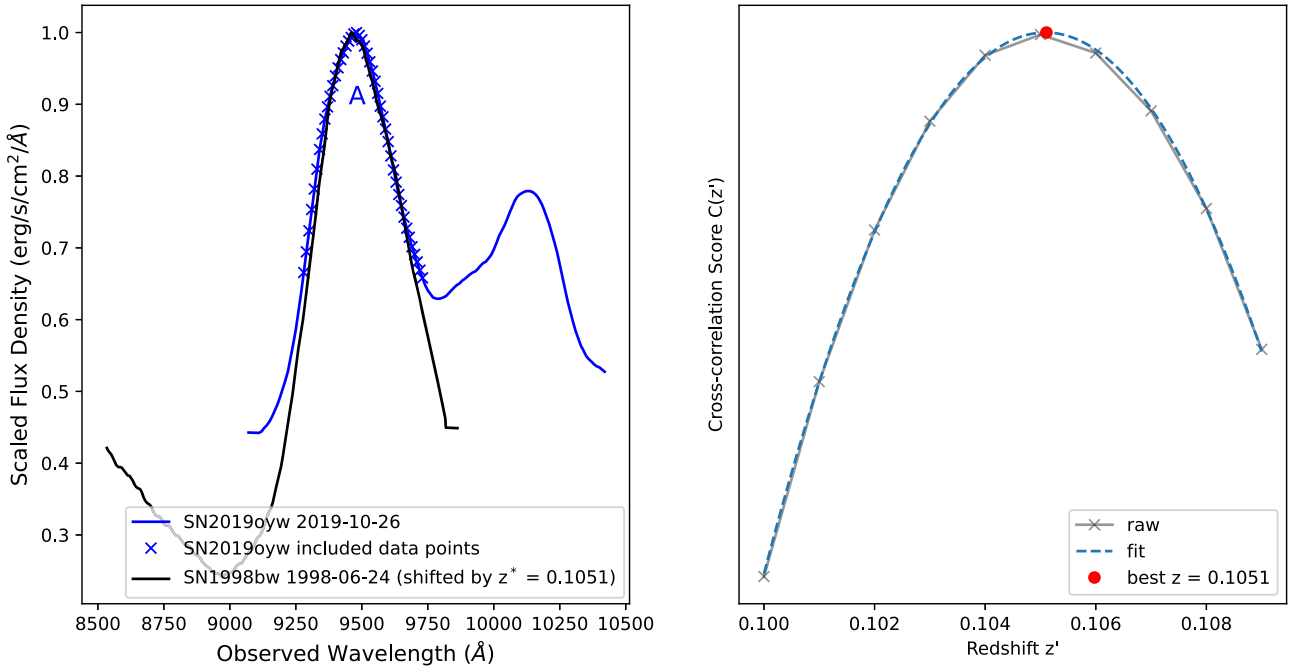

Figure 16. Cross correlation matching CaIR3 peaks. Left-hand panel: The cross-correlation technique was performed using SN 2019oyw on epoch 2019 October 26 (source, blue) and SN 1998bw on epoch 1998 June 24 (template, black). For the template, this peak was identified as CaIR3 (F. Patat et al. 2001). For the source, only included data points around the peak (blue crosses) were used in the computation. For more details, see Appendix. Right-hand panel: The optimal solution z^* from the cross correlation (red dot) is estimated by the second-order polynomial fit to the cross-correlation score curve.

direct cross correlation on the data rather than transforming to Fourier space. Both source and template spectra were extinction corrected. Following S. Blondin & J. L. Tonry (2007) both spectra were smoothed prior to cross correlation. We used the generalized Savitsky–Golay method (R. M. Quimby et al. 2018) using the same parameters as for our earlier spectral reduction (see Section 2.2 for the parameters). The template spectrum was normalized with respect to its CaIR3 peak, and the source to its feature "A." Due to limitations on the template spectrum longer than 8800 Å (rest frame) and on the source shorter than 9100 Å (observed frame), we chose to include data points surrounding the peak of the feature "A" (approximately 9300–9700 Å in the observed frame, or 8400–8800 Å in the rest frame assuming $z^* = 0.1051$ as shown in the left-hand panel in Figure 16).

We performed the cross correlation by assuming the redshift $z' \in [0.100, 0.109]$ with a step of 0.001. The cross-correlation score $C(z = z')$ showed a strictly concave profile, which was fitted by a second-order polynomial to locate the optimal solution. As shown in Figure 16, the optimal solution is $z^* = 0.1051 \pm 0.0009$, as shown in the right-hand panel in Figure 16.

ORCID iDs

Kornpob Bhirombhakdi https://orcid.org/0000-0003-0136-1281
Andrew S. Fruchter https://orcid.org/0000-0002-6652-9279
Andrew J. Levan https://orcid.org/0000-0001-7821-9369
Elena Pian https://orcid.org/0000-0001-8646-4858
Paolo Mazzali https://orcid.org/0000-0001-6876-8284
Luca Izzo https://orcid.org/0000-0001-9695-8472
Tuomas Kangas https://orcid.org/0000-0002-5477-0217
Stefano Benetti https://orcid.org/0000-0002-3256-0016
Kyle Medler https://orcid.org/0000-0001-7186-105X
Nial Tanvir https://orcid.org/0000-0003-3274-6336

References

Abdalla, H., Adam, R., Aharonian, F., et al. 2019, Natur, 575, 464
Abdurro'uf, Accetta, K., Aerts, C., et al. 2022, ApJS, 259, 35
Amati, L. 2006, MNRAS, 372, 233
ANTARES Collaboration, Albert, A., André, M., et al. 2021, JCAP, 2021, 092
Appenzeller, I., Fricke, K., Fürtig, W., et al. 1998, Msngr, 94, 1
Astropy Collaboration, Price-Whelan, A. M., Sipőcz, B. M., et al. 2018, AJ, 156, 123
Astropy Collaboration, Robitaille, T. P., Tollerud, E. J., et al. 2013, A&A, 558, A33
Ben-Ami, S., Gal-Yam, A., Filippenko, A. V., et al. 2012, ApJL, 760, L33
Blanch, O., Longo, F., Berti, A., et al. 2020, GRB Coordinates Network, Circular Service, No., 29075
Blondin, S., & Tonry, J. L. 2007, ApJ, 666, 1024
Bradley, L., Sipőcz, B., Robitaille, T., et al. 2020, astropy/photutils: v1.0.0, Zenodo, doi:10.5281/zenodo.4044744
Brown, W. R. 2015, ARA&A, 53, 15
Bufano, F., Pian, E., Sollerman, J., et al. 2012, ApJ, 753, 67
Cano, Z., de Ugarte Postigo, A., Pozanenko, A., et al. 2014, A&A, 568, A19
Chand, V., Banerjee, A., Gupta, R., et al. 2020, ApJ, 898, 42
Chornock, R., Berger, E., Levesque, E. M., et al. 2010, arXiv:1004.2262
Christensen, L., Vreeswijk, P. M., Sollerman, J., et al. 2008, A&A, 490, 45
de Naurois, M. 2019, ATel, 13052, 1
de Ugarte Postigo, A., Izzo, L., Thoene, C. C., et al. 2019, GRB Coordinates Network, Circular Service, No., 25677
Dichiara, S., Bernardini, M. G., Burrows, D. N., et al. 2019, GRB Coordinates Network, Circular Service, No., 25552
Dichiara, S., Troja, E., Lipunov, V., et al. 2022, MNRAS, 512, 2337
Dressel, L. 2021, WFC3 Instrument Handbook for Cycle 29 v.13 (Baltimore, MD: STScI)
Duan, M.-Y., & Wang, X.-G. 2019, ApJ, 884, 61
Fermi GBM Team 2019, GRB Coordinates Network, Circular Service, No. 25551
Fraija, N., Veres, P., Beniamini, P., et al. 2021, ApJ, 918, 12
Fruchter, A. S., & Hook, R. N. 2002, PASP, 114, 144
Fruchter, A. S., Levan, A. J., Strolger, L., et al. 2006, Natur, 441, 463
Galama, T. J., Vreeswijk, P. M., van Paradijs, J., et al. 1998, Natur, 395, 670
Gupta, R., Pandey, S. B., Kumar, A., et al. 2022, JApA, 43, 82
Gutiérrez, C. P., Anderson, J. P., Hamuy, M., et al. 2017, ApJ, 850, 89
H.E.S.S. Collaboration, Abdalla, H., Aharonian, F., et al. 2021, Sci, 372, 1081

Hu, Y. D., Castro-Tirado, A. J., Kumar, A., et al. 2021, A&A, 646, A50
Izzo, L., de Ugarte Postigo, A., Maeda, K., et al. 2019, Natur, 565, 324
Japelj, J., Vergani, S. D., Salvaterra, R., et al. 2018, A&A, 617, A105
Kelly, P. L., Filippenko, A. V., Fox, O. D., Zheng, W., & Clubb, K. I. 2013, ApJL, 775, L5
Kelly, P. L., Filippenko, A. V., Modjaz, M., & Kocevski, D. 2014, ApJ, 789, 23
Kewley, L. J., & Ellison, S. L. 2008, ApJ, 681, 1183
Kuemmel, M. W., Walsh, J. R., Larsen, S. S., & Hook, R. N. 2005, in ASP Conf. Ser. 347, Astronomical Data Analysis Software and Systems XIV, ed. P. Shopbell, M. Britton, & R. Ebert (San Francisco, CA: ASP), 138
Kuntschner, H., Kümmel, M., Walsh, J. R., & Bushouse, H. 2011, Revised Flux Calibration of the WFC3 G102 and G141 grisms, Space Telescope WFC Instrument Science Report
Levan, A., Crowther, P., de Grijs, R., et al. 2016, SSRv, 202, 33
Li, L., Wang, Y., Shao, L., et al. 2018, ApJS, 234, 26
Li, M., Kang, Z., Wu, C., et al. 2023, FrASS, 10, 1124317
Lipunov, V., Balakin, F., Gorbovskoy, E., et al. 2019, GRB Coordinates Network, Circular Service, No., 25652
Liu, Y.-Q., Bianco, F. B., & Modjaz, M. 2016, SESNtemple: First Public Release, v2.0, Zenodo, doi:10.5281/zenodo.58766
Lucy, L. B. 1991, ApJ, 383, 308
MAGIC Collaboration, Acciari, V. A., Ansoldi, S., et al. 2019, Natur, 575, 455
Marion, G. H., Höflich, P., Gerardy, C. L., et al. 2009, AJ, 138, 727
Mazzali, P. A., & Lucy, L. B. 1998, MNRAS, 295, 428
Medler, K. 2023, PhD Thesis, Liverpool John Moores Univ.
Modjaz, M., Bianco, F. B., Siwek, M., et al. 2020, ApJ, 892, 153
Modjaz, M., Liu, Y. Q., Bianco, F. B., & Graur, O. 2016, ApJ, 832, 108
Nakamura, T., Mazzali, P. A., Nomoto, K., & Iwamoto, K. 2001, ApJ, 550, 991
Oates, S. R., Dichiara, S. & Swift/UVOT Team 2019, GRB Coordinates Network, Circular Service, No., 25570
Patat, F., Cappellaro, E., Danziger, J., et al. 2001, ApJ, 555, 900
Perley, D. A., Krühler, T., Schady, P., et al. 2017, MNRAS, 465, L89
Perley, D. A., Niino, Y., Tanvir, N. R., Vergani, S. D., & Fynbo, J. P. U. 2016, SSRv, 202, 111
Prentice, S. J., Maguire, K., Siebenaler, L., & Jerkstrand, A. 2022, MNRAS, 514, 5686
Quimby, R. M., De Cia, A., Gal-Yam, A., et al. 2018, ApJ, 855, 2
Ravasio, M. E., Oganesyan, G., Salafia, O. S., et al. 2019, A&A, 626, A12
Sahu, Kaliash, et al. 2021, WFC3 Data Handbook v5, Baltimore: STScI
Salafia, O. S., Ravasio, M. E., Yang, J., et al. 2022, ApJL, 931, L19
Santoro, F., Kreckel, K., Belfiore, F., et al. 2022, A&A, 658, A188
Sato, Y., Obayashi, K., Theodre Zhang, B., et al. 2023, JHEAp, 37, 51
Schlafly, E. F., & Finkbeiner, D. P. 2011, ApJ, 737, 103
Schönebeck, F., Puzia, T. H., Pasquali, A., et al. 2014, A&A, 572, A13
Schulze, S., Malesani, D., Cucchiara, A., et al. 2014, A&A, 566, A102
Silverman, J. M., Vinko, J., Marion, G. H., et al. 2015, MNRAS, 451, 1973
Sim, S. A. 2017, in Handbook of Supernovae, ed. A. W. Alsabti & P. Murdin (Berlin: Springer), 769
Skrutskie, M. F., Cutri, R. M., Stiening, R., et al. 2006, AJ, 131, 1163
Srinivasaragavan, G. P., Swain, V., O'Connor, B., et al. 2024, ApJL, 960, L18
Taddia, F., Sollerman, J., Fremling, C., et al. 2019, A&A, 621, A71
Taubenberger, S., Pastorello, A., Mazzali, P. A., et al. 2006, MNRAS, 371, 1459
Toy, V. L., Cenko, S. B., Silverman, J. M., et al. 2016, ApJ, 818, 79
Valeev, A. F., Castro-Tirado, A. J., Hu, Y. D., et al. 2019, GRB Coordinates Network, Circular Service, No., 25565
van Rossum, D. R. 2012, arXiv:1208.3781
Vernet, J., Dekker, H., D'Odorico, S., et al. 2011, A&A, 536, A105
Volnova, A., Rumyantsev, V., Pozanenko, A., et al. 2019, GRB Coordinates Network, Circular Service, No., 25682
Woo, J.-H., & Urry, C. M. 2002, ApJ, 579, 530
Woosley, S. E., & Bloom, J. S. 2006, ARA&A, 44, 507
Woosley, S. E., & Heger, A. 2006, ApJ, 637, 914
Yaron, O., & Gal-Yam, A. 2012, PASP, 124, 668
Zhang, L.-L., Ren, J., Huang, X.-L., et al. 2021, ApJ, 917, 95